

A Low Pressure Turbine With Profiled Endwalls and Purge Flow Operating With a Pressure Side Bubble

P. Jenny¹

e-mail: jenny@lec.mavt.ethz.ch

R. S. Abhari

Laboratory for Energy Conversion,
Department of Mechanical and
Process Engineering,
ETH Zurich,
Zurich, 8092, Switzerland

M. G. Rose

Institute of Aeronautical Propulsion,
University of Stuttgart,
Stuttgart, 70569, Germany

M. Brettschneider

J. Gier

MTU Aero Engines GmbH,
Dachauer Strasse 665,
Munich, 80995, Germany

This paper presents an experimental and computational study of non-axisymmetric rotor endwall profiling in a low pressure turbine. Endwall profiling has been proven to be an effective technique to reduce both turbine blade row losses and the required purge flow. For this work, a rotor with profiled endwalls on both hub and shroud is considered. The rotor tip and hub endwalls have been designed using an automatic numerical optimization that is implemented in an in-house MTU code. The endwall shape is modified up to the platform leading edge. Several levels of purge flow are considered in order to analyze the combined effects of endwall profiling and purge flow. The non-dimensional parameters match real engine conditions. The 2-sensor Fast Response Aerodynamic Probe (FRAP) technique developed at ETH Zurich is used in this experimental campaign. Time-resolved measurements of the unsteady pressure, temperature and entropy fields between the rotor and stator blade rows are made. For the operating point under investigation, the turbine rotor blades have pressure side separations. The unsteady behavior of the pressure side bubble is studied. Furthermore, the results of unsteady RANS simulations are compared to the measurements and the computations are also used to detail the flow field with particular emphasis on the unsteady purge flow migration and transport mechanisms in the turbine main flow containing a rotor pressure side separation. The profiled endwalls show the beneficial effects of improved measured efficiency at this operating point, together with a reduced sensitivity to purge flow.

[DOI: 10.1115/1.4006303]

Introduction

The generic geometry of non-axisymmetric endwall profiling was proposed in the early patent of Gilbert Riollot [1], originally in Paris in 1965. Such endwalls designed 30 years later in the axial flow gas turbine context and with the benefit of 3D CFD were first proposed by Rose [2]. The profiled endwalls were designed to homogenize the endwall static pressure field at the rim seal with the aim of reducing the required turbine disk coolant mass flow. Later Hartland et al. [3] and Ingram et al. [4] showed in the Durham linear cascade that significant secondary loss reductions can be achieved using non-axisymmetric endwalls. Brennan et al. [5] and Rose et al. [6] redesigned the endwalls of an HP turbine model rig and reported an increase in stage efficiency of 0.4% from computations and $0.6\% \pm 0.25\%$ from measurements. Duden et al. [7] investigated the combined effects of blade thickening and endwall contouring. Praisner et al. [8] have confirmed that endwall contouring is an effective method for reducing endwall losses in a high-lift airfoil cascade using a CFD based endwall optimizer. Schuepbach et al. [9] performed measurements with the model axial turbine test rig used for the current experimental measurement campaign and reported an efficiency improvement of $1.0\% \pm 0.4\%$ due to the non-axisymmetric endwalls designed by Germain et al. [10]. The improvement was mainly found in the nozzle guide vane and was due to a significant reduction of the secondary flow losses as well as a substantial reduction in mid-span losses.

The secondary cooling mass flow considered for this work is the purge flow injected at the rim seal between the nozzle guide vane and rotor. The purge flow prevents the ingestion of hot gases

into the disk cavities in order to prevent the disk's overheating and to avoid thermal fatigue. Therefore, bypassed compressor air is injected through the rim seals between the rotating and stationary parts. The ingestion of hot gases is driven by disk pumping and the external non-axisymmetric static pressure field. This has been experimentally investigated in previous studies. Kobayashi et al. [11] found that the pressure difference criterion underestimated the minimum cooling flow rate. Chew et al. [12] and Dadkhah et al. [13] analyzed the minimum required coolant flow required for different rim seal shapes and compared this to the differential pressure criterion. The strong effect of injected cooling air on the development of the secondary flow structures has been reported in the open literature. McLean et al. [14] experimentally tested "radial, impingement and root injection" cooling configurations as defined in Ref. [14]. They found the three-dimensional secondary flow structure and stage performance to be significantly affected by the cooling mass flow. Ong et al. [15] found that the introduction of a swirl component to the coolant jet reduces the efficiency penalty caused by the coolant due to a reduction in viscous dissipation and secondary flow strength. Furthermore, they found that most of the coolant is entrained by the downstream blade hub secondary flow. Paniagua et al. [16] reported that there is an intensification of the rotor hub vortex and an enhancement of the radial migration due to injection in a transonic high pressure turbine. Reid et al. [17] quantified the efficiency penalty caused by the rim seal flow as being about 0.56% per percent of injection mass flow. The effect of the blade leading edge platform was investigated in a numerical study by Marini and Girgis [18]. They presented a design offering a 0.07% stage efficiency benefit and a reduced sensitivity to an increasing cavity mass flow. Schuepbach et al. [19] have shown a 0.6% efficiency drop for 0.9% purge flow with axisymmetric endwalls. Additionally, intensification of the secondary flows at the exit of the rotor as well as a higher penetration of the secondary flows with purge flow were observed.

¹Corresponding author.

Contributed by the International Gas Turbine Institute (IGTI) of ASME for publication in the JOURNAL OF TURBOMACHINERY. Manuscript received July 25, 2011; final manuscript received July 27, 2011; published online September 17, 2012. Editor: David Wisler.

For cost reasons, in most applications, low-pressure turbine blades are thin and solid. Because of their small leading edge radius, low pressure turbine blades often have separated flow on the pressure side. The behavior of the separation bubble is complex and highly unsteady. Brear et al. [20] quantified the loss produced by a pressure side bubble in a linear cascade, showing that it can be a significant contributor to the profile loss. They also found the incidence to be the controlling parameter for the characteristics of the pressure side separation. Similar findings were reported by Yamamoto et al. [21] and Hodson et al. [22]. The migration process of the separated fluid was first studied by Brear et al. [23] proposing a strong interaction with the hub secondary flows.

This paper experimentally quantifies the flow and interaction mechanisms involved between purge flow and profiled endwalls in a shrouded low pressure turbine rotor operating with pressure side separations. The time-resolved measurements are made in a rotating model axial turbine and compared to the results of a high-fidelity numerical model. The profiled endwalls were designed to mitigate the effect of purge flow.

Experimental Method

The experimental investigation was performed in the “LISA” research turbine at the Laboratory for Energy Conversion (LEC) at the Swiss Federal Institute of Technology in Zurich.

Experimental Turbine Facility. The air-loop of the facility is quasi-closed and includes a radial compressor, a two-stage water to air heat exchanger and a calibrated venturi nozzle for mass flow measurements. Upstream of the turbine section is a 3 m flow conditioning stretch to ensure a homogenous flow field. Additionally, the flow undergoes acceleration ahead of the turbine section in order to reduce the significance of remaining flow non-uniformities from upstream. At the exit of the turbine section, the air loop opens to the atmosphere. A DC generator absorbs the turbine power and controls the rotational speed with an accuracy of $\pm 0.02\%$ (± 0.5 RPM). A heat exchanger controls the inlet total temperature $T_{t,in}$ to an accuracy of $\pm 0.3\%$. A torque meter measures the torque on the rotor shaft. With the compressor ratio limited to $\Pi_{c,max} = 1.4$, it is necessary to add a tandem de-swirl vane arrangement to recover the static pressure at the exit of the second stator back to the ambient level, in order to reach the intended turbine total-to-static pressure ratio of $\Pi_{1,5} = 1.65$. At the exit of the first nozzle guide vane row, the flow is compressible with an exit Mach number of 0.53.

Operating Conditions. During all measurements, the turbine 1.5 stage total-to-static pressure ratio is kept constant at $\Pi_{1,5} = 1.65$ and the total turbine entry temperature is kept uniform at $T_{t,in} = 328$ K. In order to account for the change in ambient pressure on different measurement days, the pressures are non-dimensionalized by the respective inlet total pressure. These operating conditions are in agreement with measurements previously obtained using this turbine and permit an accurate comparison between measurements made on different days. See Table 1.

Injection System. The air injected through the rim seal between the nozzle guide vane and rotor is bled off the primary air-loop upstream of the main flow conditioning stretch. The mass flow of the bypassed air is measured by means of a venturi, which is part of the auxiliary air system. After having passed a plenum the air is fed into the rim seal cavity through tunnels inside 10 different nozzle guide vanes, labeled **B** in Fig. 1, which illustrates the leakage path and the rim seal cavity.

From the cavity underneath the nozzle guide vanes, there are two leakage paths, which are indicated in Fig. 1 as dotted arrows **P** and **S**. One path is through the upstream rim seal into the main flow, **P**. The rest of the gas, called the secondary mass flow **S**, is ejected through the drum to ambient conditions after being measured in another venturi. The pressure difference over the labyrinth seal between the downstream rim seal and the drum is balanced. Under these conditions the net mass flow through the downstream rim seal into the drum is assumed to be zero. Thus the injected mass flow can be calculated as the difference between the measured bypass and the secondary mass flows. The injection rate (*IR*) is defined as the ratio between the injected mass flow and the total turbine mass flow, given by Eq. (1):

$$IR = \frac{\dot{m}_{bypass} - \dot{m}_{drum}}{\dot{m}_{main}} \quad (1)$$

Table 1 Operating conditions and geometrical characteristics

$\Pi_{1,5}$	$1.65 \pm 0.4\%$ [-]
$T_{t,in}$	328 ± 0.2 [K]
$\frac{\dot{m}\sqrt{T_{t,in}}}{P_{t,in}}$	$152 \pm 0.2\%$ $\left[\frac{kg\sqrt{K}}{s \cdot bar}\right]$
$\frac{N}{\sqrt{T_{t,in}}}$	2.48 ± 0.05 $\left[\frac{r.p.s.}{\sqrt{K}}\right]$
Mach (S1ex/R1ex/S2ex)	0.52/0.28/0.48 [-]
Re (S1/R1/S2)	$7.1/3.8/5.1 \cdot 10^5$ [-]
Blade count (S1/R1/S2)	36/54/36 [-]
Aspect ratio (S1/R1/S2)	0.87/1.17/0.82 [-]

used in another venturi. The pressure difference over the labyrinth seal between the downstream rim seal and the drum is balanced. Under these conditions the net mass flow through the downstream rim seal into the drum is assumed to be zero. Thus the injected mass flow can be calculated as the difference between the measured bypass and the secondary mass flows. The injection rate (*IR*) is defined as the ratio between the injected mass flow and the total turbine mass flow, given by Eq. (1):

The measurements were conducted with the following three different injection rates: $IR = 0.4\%$, $IR = 0.8\%$, and $IR = 1.2\%$, which are representative of low, nominal, and high injection rates.

Endwall and Airfoil Design Methodology. The existing 2-stage, shrouded turbine configuration was initially redesigned as a one-and-half stage unshrouded turbine representative of a high work, cooled, high-pressure turbine. Further details of this design are presented by Behr et al. [24]. For the current experimental study, the rotor of the one-and-half stage configuration was replaced by a shrouded rotor with thinner airfoils more representative of a low-pressure rotor. The nozzle guide vane also has shaped endwalls. The main features and the methodology of the corresponding endwall design have been presented by Germain et al. [10]. The primary objectives of the nozzle guide vane endwall optimization are to reduce secondary kinetic energy and to

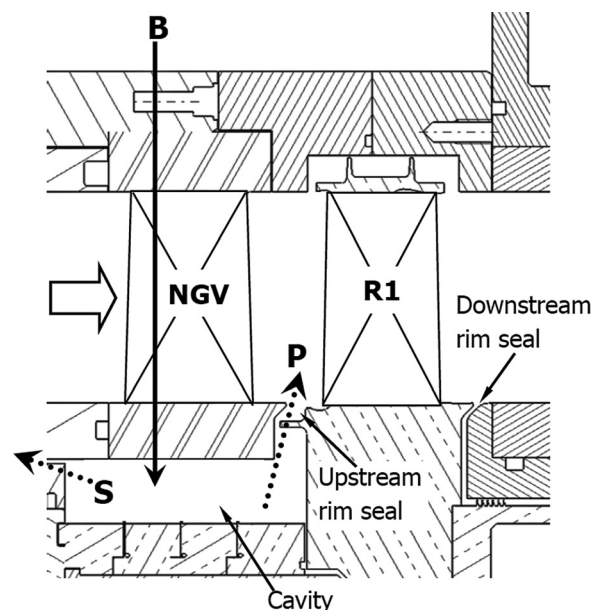


Fig. 1 Illustration of leakage path

improve row efficiency. The modified secondary kinetic energy definition is presented in Germain et al. [25]. The rotor endwall contour design is the result of a three-dimensional endwall optimization algorithm taking into account purge flow as well as the rim seal and the rotor shroud cavity geometries. The optimization was performed for nominal operating conditions with a nominal purge flow rate of 0.8% of the main mass flow. A constant flow capacity was imposed as a boundary condition for the optimizer. Rotor tip and hub endwalls have been designed using automatic numerical optimization by means of a gradient based MTU-in-house optimizer code, the flow being computed by the steady 3D RANS solver TRACE developed at DLR and MTU. The aim of the rotor endwall design was to mitigate the effect of purge flow and to reduce the secondary losses and secondary kinetic energy. The optimizer modified the endwall shape up to the rotor hub platform leading edge and not only between the leading and trailing edges. The result of the endwall profiling optimization is shown in Fig. 2 for the NGV and rotor hub and tip endwalls. The NGV hub endwall has a typical suction side trough and higher amplitudes compared to the corresponding rotor hub and tip endwalls. The amplitudes at the rotor tip must remain within the thickness of the rotor shroud. The profiling at the rotor hub platform goes up to the leading edge, giving it a wavy shape.

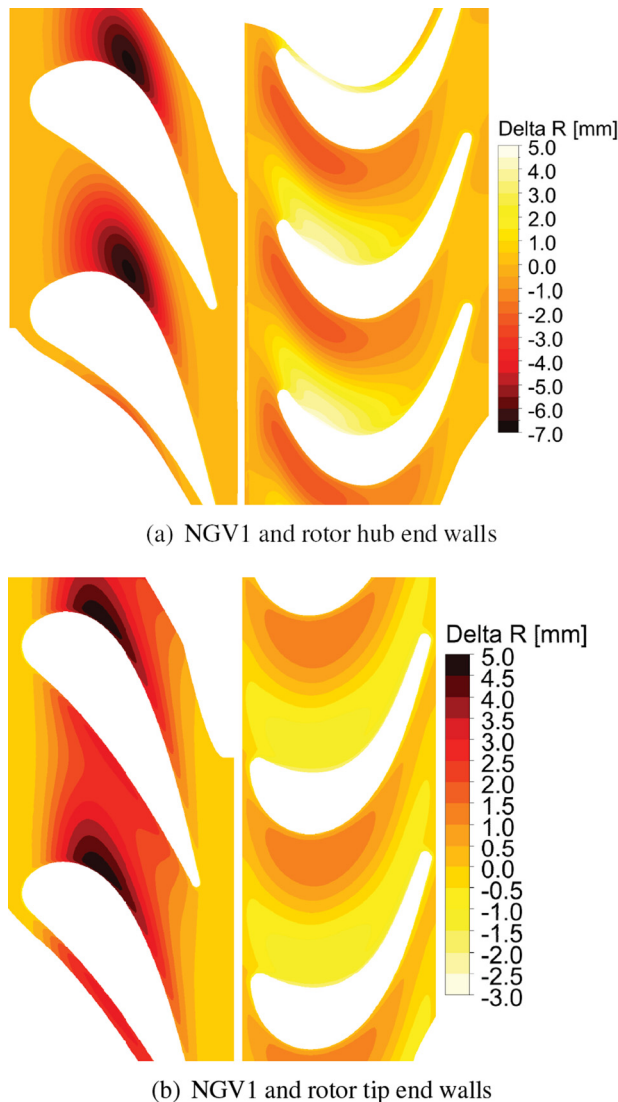


Fig. 2 Non-axisymmetric endwall shapes from the optimization

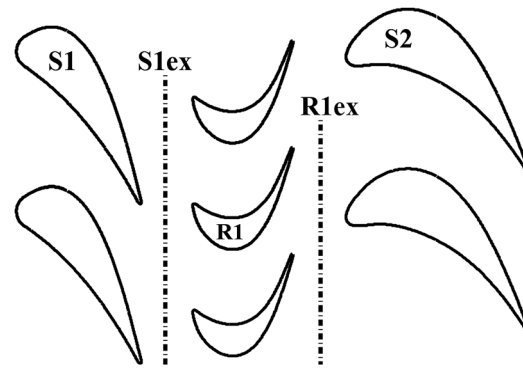


Fig. 3 Illustration of geometrical relations and measurement planes

Measurement Planes. The data was measured at two different traversing planes in the turbine test facility. Figure 3 shows the blade rows and relative positions of the two traverse planes S1ex and R1ex. At traverse planes S1ex and R1ex, the spatial resolution of the measurement grid consisted of 42 radial and 41 equally spaced points in the circumferential direction covering one stator pitch. The measurement grid shows radial clustering near the endwalls.

Measurement Technology. The unsteady flow field was measured using a standard Fast Response Aerodynamic Probe (FRAP) developed at the ETH Zurich (Kupferschmied et al. [26] and Pfau et al. [27]). It is capable of capturing unsteady flow features up to frequencies of 48 kHz based on measurements including total and static pressures, flow yaw and pitch angles and Mach number. The frequency bandwidth of the temperature is limited to a frequency of 10 Hz. However, the influence of the measured temperature on the velocity is very modest. The standard FRAP probe has a 1.8 mm tip diameter and is equipped with two sensors. The probe is operated in a virtual-4-sensor mode to measure three-dimensional, time-resolved flow properties. Table 2 gives the relative measurement uncertainties of the FRAP probe as a percentage of the calibration range of ± 24 deg for the yaw angle, ± 20 deg for the pitch angle and as a percentage of the dynamic head for the total and static pressure. The data is acquired at a sampling rate of 200 kHz over a period of 2 s. The post-processing is done for three consecutive rotor pitches. The sampling rate resolves 82 points per rotor pitch. During these 2 s, the three blade passing events are phase-lock-averaged 85 times.

Time-Resolved Computational Model

Grid and Boundary Conditions. The grid used for the time-resolved simulations is structured and has a total of 18.5×10^6 nodes. As the blade count ratio between stationary and rotating blade rows is two to three, two vane passages of the first and second vane rows as well as three rotor passages are represented in the mesh with periodic boundary conditions in the circumferential direction. In order to have a realistic rim seal flow field, the cavity space of the test rig configuration between rotor disk and first vane row is fully modeled with an interface to the first NGV exit hub endwall (Fig. 1). The non-dimensionalized wall distances on the airfoils and the endwalls are on average $y^+ = 1.5$. At the inlet of the turbine domain, a constant total pressure and total

Table 2 Relative uncertainty of FRAP probe

Yaw angle	Pitch angle	P_t	P_s
0.8%	2.3%	1.0%	1.2%

temperature corresponding to the measured experimental operating conditions were applied. At the exit the measured mass flow at these inlet conditions was imposed as a boundary condition. The purge mass flow rate, measured static pressure and temperature were imposed as boundary conditions at the cavity inlet.

Solver. In contrast to the design calculations, the time-resolved results were achieved with the commercial ANSYS CFX Version 12.1 software package. The results of a steady run were used as initial conditions for the time-resolved simulation. The temporal resolution is 80 time steps per period, corresponding to three rotor blade passing events, or a 0.25 deg shift of the rotor per time step. The shear stress transport (SST) turbulence model without transition modeling was used for the simulations. The maximum residuals were found to be in the order of 10^{-3} , while the mass imbalances were in the order of 10^{-5} . The periodic convergence of the unsteady simulations was judged based on the correlation coefficient of two pressure monitoring points at the rotor exit. Two consecutive vane passage pressure events had to reach a correlation coefficient of over 99%.

Validation. In order to validate the computational model, the time-averaged results of the unsteady CFD calculation are compared to the experimental results. The validation is done for all the experimentally investigated injection rates. Figure 4 shows the comparison between the measurement and the numerical prediction of the circumferentially mass and time-averaged radial distribution of the relative flow angle at the rotor exit for the nominal injection rate of $IR = 0.8\%$. The absolute difference in relative flow angle is within 4 deg below 90% span. The loss cores are detected at the same radial positions by the CFD simulation and are of a similar shape and strength. The fact that the radial position of the hub loss core is very well captured by the simulation is relevant for the analysis presented. Figure 5 compares the measured and computed time-averaged normalized total pressure at the rotor exit in the rotor frame of reference. A good qualitative agreement between computational prediction and measurement was achieved with regard to the shape and radial position of the zones of low total pressure caused by the hub and tip secondary flows. Generally speaking, the CFD simulation appears to over-predict the losses compared to the measured data. In the free-stream region, the maximum relative error of the relative total pressure between simulation and measurement is about 0.5%. The hub passage vortex and rotor wake loss cores are under-predicted by the computation by about 2%. In the tip region over 90% span the relative error reaches about 3%.

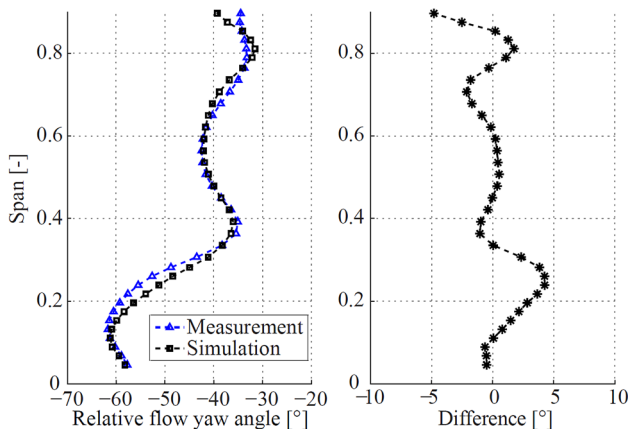


Fig. 4 Comparison between measured and simulated relative flow yaw angle at rotor exit for the nominal injection rate ($IR = 0.8\%$)

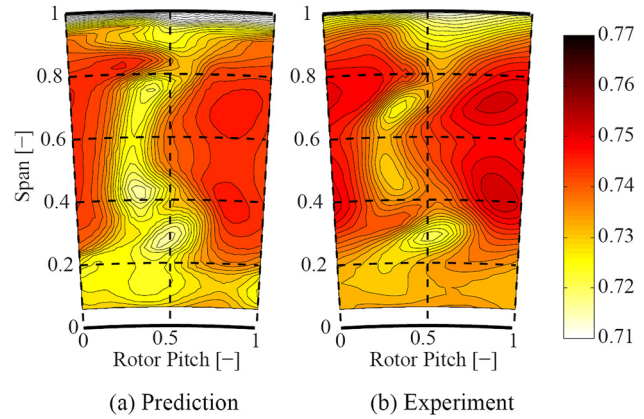


Fig. 5 Comparison of normalized total pressure ($=P_t/P_{t,in}$) in rotor frame of reference for prediction and experiment at the rotor exit at the nominal injection rate $IR = 0.8\%$

Results and Discussion

In the following section, the time-resolved flow field data are presented with particular attention to the unsteady interaction mechanisms between purge flow and endwall profiling. The analysis starts with a discussion of the measurement results at rotor exit for three different injection rates. Corresponding CFD simulations will complement the analysis by providing information on the rotor flow field—at locations that are inaccessible for the probe measurement technique used.

Sensitivity of Efficiency to Purge Flow. In this section, the effect of injected purge flow on efficiency is analyzed. Probe measurements at rotor exit are considered. The definition of total-to-total efficiency accounting for the injection used in this study is given in Eq. (2):

$$\eta_{tt} = \frac{\frac{\omega M}{\dot{m} C_p T_{t,in}}}{1 - \left(1 - \frac{IR}{100}\right) \left(\frac{p_{t,R1ex}}{p_{t,in}}\right)^{\frac{\gamma-1}{\gamma}} - \frac{IR}{100} \left(\frac{p_{t,R1ex}}{p_{t,Cavity}}\right)^{\frac{\gamma-1}{\gamma}}} \quad (2)$$

Figure 6 shows the measured and simulated normalized total-to-total efficiency as a function of injected purge flow. The decrease in efficiency with increasing injection rate is very linear for the measurements—the total-to-total efficiency decreases by 1.3% per percent of injected purge flow. Schuepbach et al. [9] reported a 1.2% decrease of total-to-total efficiency per percent of injected fluid using the same NGV as in the present experiment

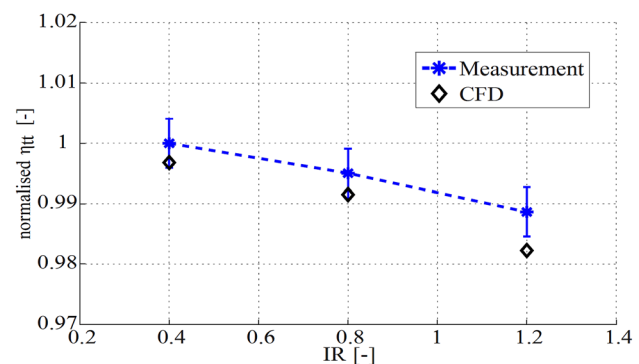


Fig. 6 Normalized total to total efficiency as a function of injected purge flow for computation and measurements with error estimation

but an unshrouded rotor with high pressure turbine representative airfoils. The data from the computational model show the same sensitivity to purge flow between low and nominal injection rate. However, the computed sensitivity slightly increases for higher blowing rates. Compared to the measurements, the computed efficiency is 0.3% lower for the lowest injection rate and 0.55% lower for the highest injection rate in absolute terms. Compared to a baseline measurement with the same blade geometry and cylindrical endwalls, the measured total-to-total efficiency has increased by 0.8% on an absolute scale due to the beneficial effect of the shaped endwalls for nominal injection rate. Furthermore, the end-wall design presented has also reduced the sensitivity of efficiency to purge flow by 18% compared to the baseline case. A similar trend was reported by Schuepbach et al. [9].

Unsteady Purge Flow Migration in Rotor Flow Field. Figure 7 shows the radial distribution of the mass and time-averaged relative flow yaw angle at the exit of the rotor for the three injection rates investigated. The injected purge flow only has an effect on the flow field below 65% span. Above this radial position, the flow field is unaltered by the purge flow for the turbine configuration tested. The strong variations of yaw angle between 10% and 50% span are caused by the hub secondary flows and are indicative of streamwise vorticity. Increased injection flow causes the secondary flow structure to radially migrate outwards by about 5 to 10% span. Similar findings have been reported by Schuepbach et al. [19] and Ong et al. [15].

Another way of observing the influence of purge flow on the flow field is to analyze the experimentally evaluated root mean square values (rms) of the total pressure random part at rotor exit. Regions of high rms are indicative of significant non-deterministic unsteadiness. This may be due to flow instability modes, e.g., eddy shedding or transition or may be simply due to high turbulence. Using the triple decomposition of the time-resolved pressure signal as shown in Eq. (3), the random part $p'(t)$ can be evaluated as the difference between the raw pressure $p(t)$ signal of the FRAP probe and the phase-locked averaged pressure $p_{-+} \sim p_{-}(t)$. The same approach was used by Porreca et al. [28] to derive turbulent quantities.

$$p(t) = \bar{p} + \tilde{p}(t) + p'(t) \quad (3)$$

Figure 8 shows the experimental time-averaged rms distribution of the total pressure random part in the rotor frame of reference at rotor exit for the lowest and highest investigated injection rates. The tip region shows zones of elevated rms over the whole circumference, an indication of fluid leaving the shroud cavity

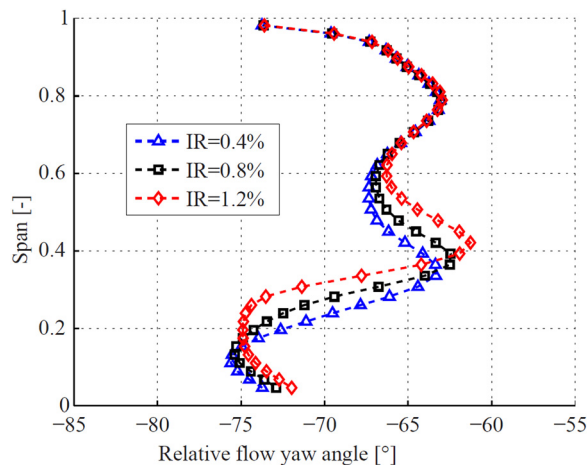


Fig. 7 Radial distribution of circumferentially mass and time-averaged measured relative flow yaw angle at rotor exit as a function of injection rate

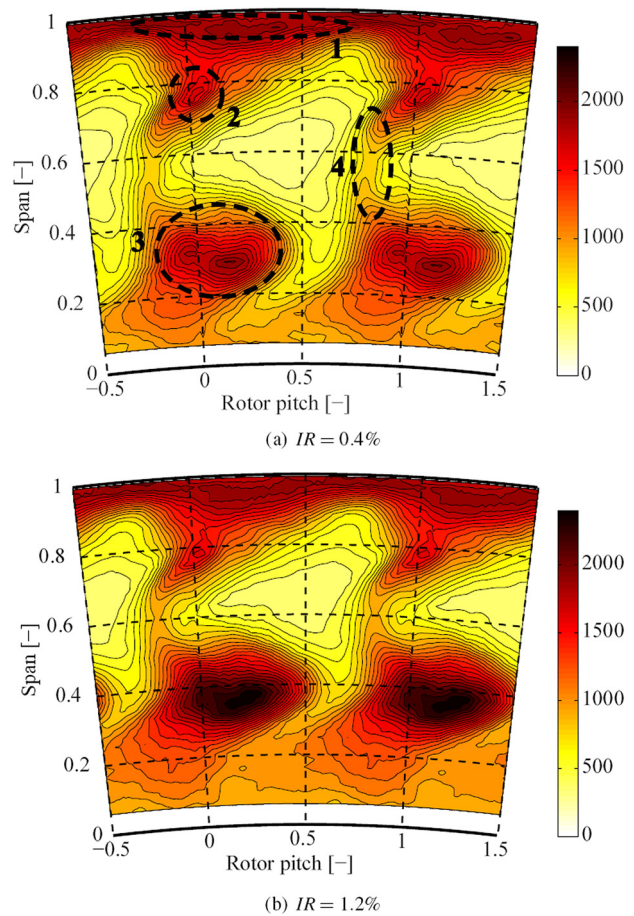


Fig. 8 Time-averaged area plot in rotor relative frame of reference at rotor exit. The parameter is the experimental rms of the rotor relative total pressure $P_{t,rel}$ (Pa).

(zone 1). The high rms feature at about 75% span represents the tip passage vortex (zone 2). The significant loss core between 30% and 40% span is the signature of the hub passage vortex (zone 3). The zones of increased rms between the tip passage and hub passage vortex are caused by the rotor wake (zone 4). In contrast to the hub vorticities, the tip structures are not influenced by the injected purge flow. The flow field structure does not significantly alter with the addition of more purge flow. The free stream region between the rotor wakes and secondary flow structures remains unaffected by the injected purge flow. However, the peak rms unsteadiness in the hub passage loss core becomes much stronger. The maximum measured rms value in the hub passage vortex increases by 25% if the purge flow level is increased from $IR = 0.4\%$ to $IR = 1.2\%$. The increased level of rms in the loss core for higher injection flow indicates where the injected purge flow migrates to at the rotor exit. The injected fluid interacts with the hub secondary flows, ending up in the core of the passage vortex where it increases the unsteadiness. A mass-weighted integral of the rms distribution between 10% and 60% span shows a 40% higher value for the high injection rate than for the low injection rate per percent of injected purge flow. Considering an integral over one entire rotor pitch, the overall level of rms increases by about 20% per percent of injected fluid.

Figure 9 shows the time-averaged streamwise vorticity Ω_s at rotor exit in the rotor frame of reference for the maximum and minimum purge flow rates. The streamwise vorticity is the scalar product of the vorticity vector and the primary flow vector. The required axial gradients are approximated using a frozen flow structure assumption. The detailed approach and calculation can be found in Schuepbach et al. [9]. The comparison of the plots for

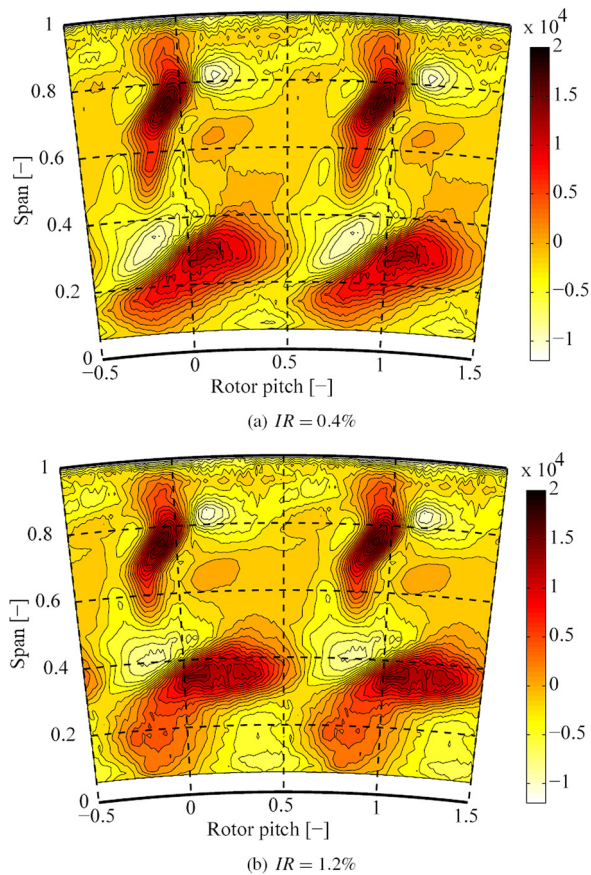


Fig. 9 Time-averaged area plot in rotor relative frame of reference at rotor exit. The parameter is the streamwise vorticity Ω_S (1/s).

the two injection rates in Fig. 9 shows that the peak vorticity in the loss core does not increase with purge flow. In order to compare the two hub passage vortical structures, the circulation has been calculated by integrating the streamwise vorticity over the area covered by the hub passage loss core. The streamwise vorticity inside an iso-contour of zero vorticity has been considered. The difference in circulation inside the iso-contour of zero streamwise vorticity between high and low purge flow levels is about 8%. To summarize, there is a significant increase in rms due to turbulence of the flow in the loss core region but not much of an increase in streamwise vorticity.

A more detailed picture can be drawn when considering absolute frame time space diagrams at the rotor exit. Figure 10 shows a space time diagram of the random part of the experimental rms signal at 60% span at the rotor exit. Figure 10(a) gives the lowest injection rate and Fig. 10(b) the highest. These plots are at the highest spanwise position (60%) to be influenced by the purge flow, at this height the flow is not dominated by the hub loss core. In both diagrams, there are a series of rounded high rms patches stacked vertically at about -0.15 stator pitch. These are the signature of the upstream NGV1 wake, a stationary feature with regard to space but fluctuating in time. Whereas the inclined high rms features are caused by the rotor wakes, the NGV and rotor wakes are very similar in the two time space plots in Fig. 10, showing that the operating point was very similar. However, at about 40% to 50% stator pitch, the plot for the higher injection rate shows a region of increased rms signal indicated by the dashed lines in Fig. 10. The difference between the two time space plots must be caused by the injected fluid because this is the only significant change. As the injected fluid is increased, the purge mass flow collects on the rotor suction side, which is what the probe sees first when the rotor blade is passing by. Therefore the increase in rms

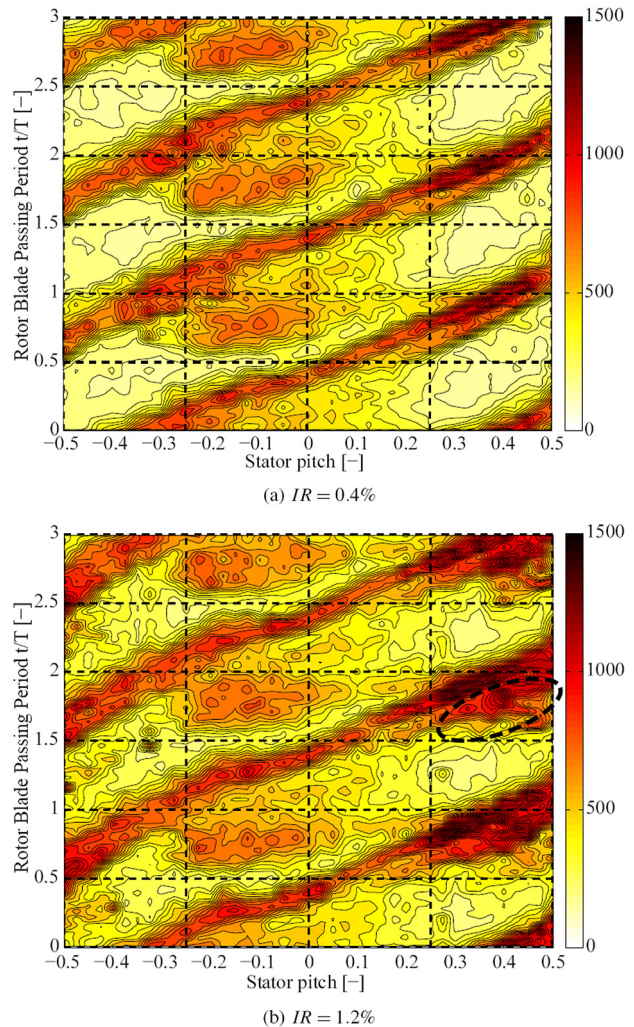


Fig. 10 Time space plot of the experimental rms of the total pressure (Pa) at 60% span

is on the lower side of the rotor wake on the time space plots in Fig. 10. Furthermore, the high rms due to the injected fluid is concentrated around one circumferential region, suggesting that the trajectory of the purge fluid is influenced by something stationary—probably the upstream vane. The NGV interaction is causing the injected fluid to interact with the suction side of the rotor at a fixed point in absolute space. The jet of injected fluid pulsates in the relative frame of reference, one burst of flow per NGV passing event.

Pressure Side Bubble Behavior in Rotating Blade Row. In addition to the flow measurements, an unsteady computation was performed in order to better understand the rotor flow field at locations inaccessible for the probes. The airfoil design features a small leading edge radius and very high turning and loading. At the simulated operating point, the inner region of the pressure side is found to be separated at the lower span positions.

Figure 11 shows iso-surfaces of zero axial velocity on the rotor blade pressure side for 10 equally spaced snapshots during one period. Due to the 2 to 3 blade count between NGV and rotor, one period corresponds to two NGV pitches. Therefore, each rotor blade interacts with two NGV wakes during one period and the potential field interaction also goes through two cycles. The time-resolved CFD simulations clearly detect a separation bubble in the hub region close to the leading edge on the rotor pressure side. The size of the pressure side separation shows very unsteady behavior. During one period, the bubble disappears twice and builds up again

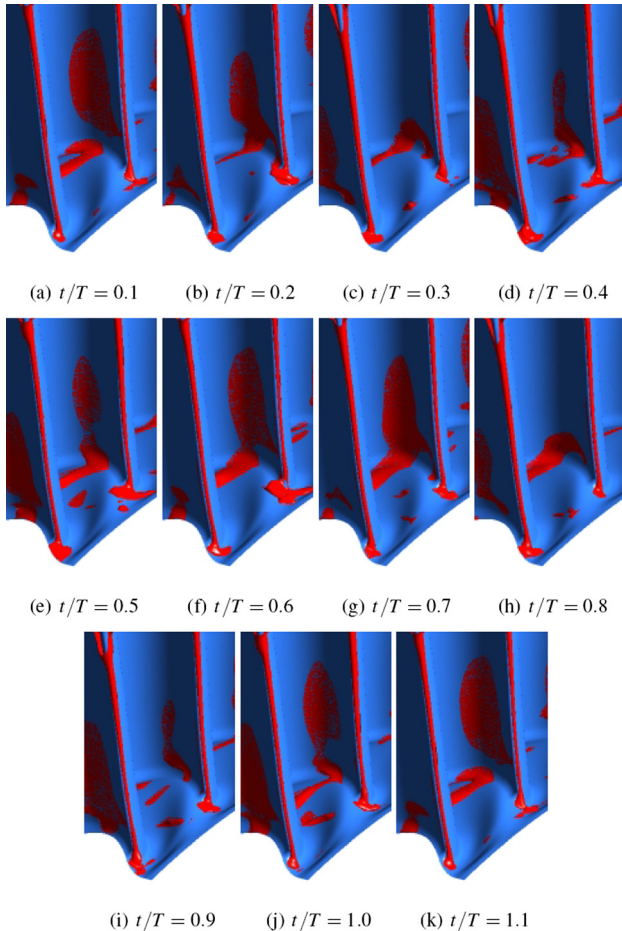


Fig. 11 Iso-surfaces of zero axial velocity on the rotor blade pressure side during one period T corresponding to two stator pitches. The black rectangle in Fig. 13 defines the view of each subfigure.

after having disappeared. During one period, the NGV wake hits the rotor blade row twice; therefore there may be a link between the two elements. The iso-surfaces not only reveal a bubble on the pressure side, but also a vortical structure on the hub endwall. This vortical structure can be described as an unsteady endwall separation and it appears to act like a tube draining the fluid periodically from the pressure side separation. The size of this structure on the hub endwall seems to be related to the size of the pressure separation. When the pressure side bubble decreases in size the structure on the hub endwall is very big (time step $t/T=0.1$ or $t/T=0.6$ on Fig. 11) and disappears when the pressure side bubble grows again ($t/T=0.4$ or $t/T=0.9$). The pressure side bubble seems to get purged through this vortical structure on the hub endwall once per nozzle guide vane passing event.

In order to get a more detailed view of the flow physics related to the separation bubble, a particle tracking code was implemented using the 3rd order Adams-Bashforth algorithm with 4 sub-iterations [29]. Based on the CFD results for each time step, the algorithm computes the next position based on the actual location and the velocity vectors at this actual location at the actual and two former time steps. Particles were released inside the pressure bubble at one specific point in time. Figure 12 shows the computed particle tracks of six particles that were released inside the pressure side bubble. The color of the particles indicates the relative velocity of the particles. The particles released inside the pressure bubble migrate slowly and radially towards the hub. The pressure side bubble fluid is of low relative momentum and therefore skews towards the region of low reduced static pressure in rotating systems. The

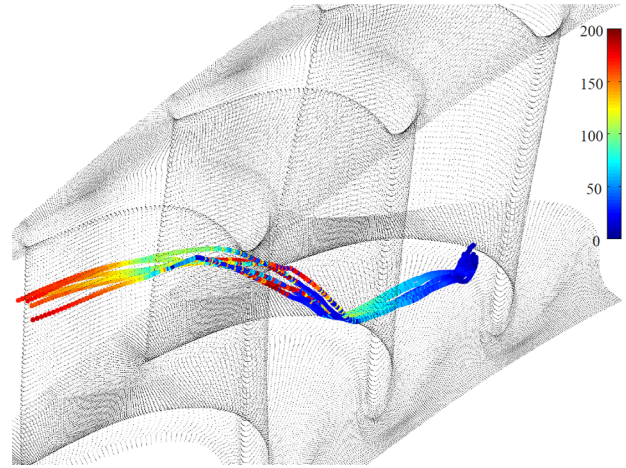


Fig. 12 Particle tracks of particles released inside pressure side bubble, $IR = 0.8\%$. The color of the particles indicates the relative velocity (m/s).

reduced static pressure is known from literature (Moore et al. [30], Greitzer et al. [31]), and is defined in Eq. (4):

$$P_{\text{red}} = P_s \left(\frac{2C_p T_s + (V_{\text{rel}}^2 - U^2)}{2C_p T_s + V_{\text{rel}}^2} \right)^{\frac{\gamma}{\gamma-1}} \quad (4)$$

On the rotor blades and endwalls, the relative velocity is zero ($V_{\text{rel}} = 0$). Equation (4) can therefore be rewritten as:

$$P_{\text{red}} = P_s \left(1 - \frac{U^2}{2C_p T_s} \right)^{\frac{\gamma}{\gamma-1}} \quad (5)$$

Figure 13 shows the contour plots of computed reduced static pressure on the rotor pressure side for one specific time step. It can be seen that the radial gradient of the reduced static pressure is outwards at the hub on the third rotor blade. This drives the stagnant bubble fluid radially inwards. Particles on the pressure side above the region of maximum reduced static pressure experience an opposite gradient and migrate towards the tip. It is also important to note that this radial gradient is not steadily present. It is a function of the relative position of the stationary and rotating blade rows. The reduced static pressure that drives the bubble migration is set up by the bubble itself, its size and shape depends on the distribution of reduced static pressure (Fig. 11). A feedback

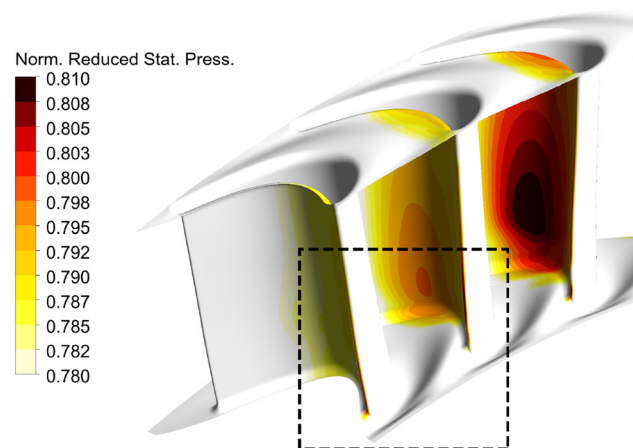


Fig. 13 Contour plot of normalized reduced static pressure ($=P_{\text{red}}/P_{t,\text{in}}$) on the rotor blade for nominal injection rate

mechanism seems to exist and the bubble blockage changes the reduced static pressure which causes the bubble fluid to migrate.

The endwall profiling introduced a convex region of curvature near the pressure side endwall corner. This is a feature that is typically present in successful non-axisymmetric endwall profiling. The effect is to reduce the static pressure in this region, tending to reduce the cross-passage pressure gradient. This effect also acts to attract the pressure side separation fluid down the blade and onto the endwall, as shown by the computed particle tracks in Fig. 12. The vortical structure on the hub endwall in Fig. 11 forms a tunnel for the pressure side separation bubble particles to travel across the passage. As the pressure side separation fluid has low momentum, it responds to the cross passage pressure gradient. Once the particles arrive at the suction side, they interact with the suction side secondary flows and get rolled up. The main flow has to transfer work to these particles in order to accelerate them, creating loss to the flow. A similar mechanism has been presented by Brear et al. [23] for low pressure turbine blades in a linear cascade.

Purge Flow Interaction With Pressure Side Separation. The size and shape of the pressure side separation depends on the amount of injected fluid. The unsteady behavior between the separated pressure side and the injected purge flow is analyzed next. Figure 14 shows the computed iso-surface of zero axial velocity on the rotor pressure side for the three different levels of injection investigated. Generally speaking, the bubble grows with increasing rate of injection. At higher injection rate, the mass flow going through the rotor throat increases. As a consequence, the Mach number at the throat has to increase, assuming a constant throat area and the rotor exit static pressure does not change. The rotor is not choked in the present experimental setup. This causes increased throat mass flow and allows the purge flow and the rest of the turbine flow through without any significant reduction of the turbine mass flow. Therefore the static pressure at rotor inlet and the reaction increase for higher injection rates, raising the relative total pressure at the rotor inlet. Figure 15 shows this increase in static pressure for higher injection rates based on the measurement results at rotor inlet. The static pressure increases by 1% per percent of injected flow in the hub region at rotor inlet. If the static pressure increases at rotor inlet, the absolute Mach number decreases, causing negative incidence on the rotor leading edge. Figure 15 shows the circumferentially area and time-averaged measured change of incidence at the rotor inlet between the nominal injection rate ($IR=0.8\%$) and the lowest injection rate ($IR=0.4\%$) and the maximum injection rate ($IR=1.2\%$) and the lowest injection rate. For the higher span-wise positions in the free stream, the difference is between -1 deg and -2 deg. Close to the hub the maximum measured difference of relative flow yaw angle between the lowest and highest injection rate peaks at about -9 deg. The missing swirl of the injected purge flow compared to the free stream mainly causes the difference in relative flow yaw angle close to the hub. The relatively thin rotor blade profiles do not tolerate a negative change in incidence well and as a consequence the bubble becomes bigger. The strong dependence of the

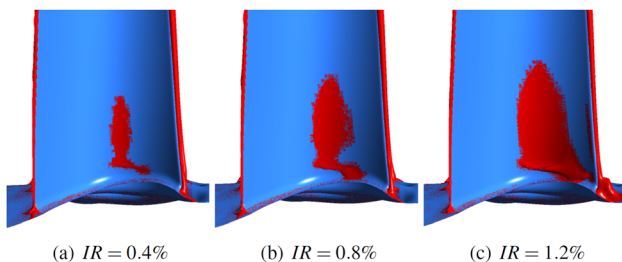


Fig. 14 Iso-surfaces of zero axial velocity on the rotor blade pressure side for three different injection levels but at the same phase in the cycle

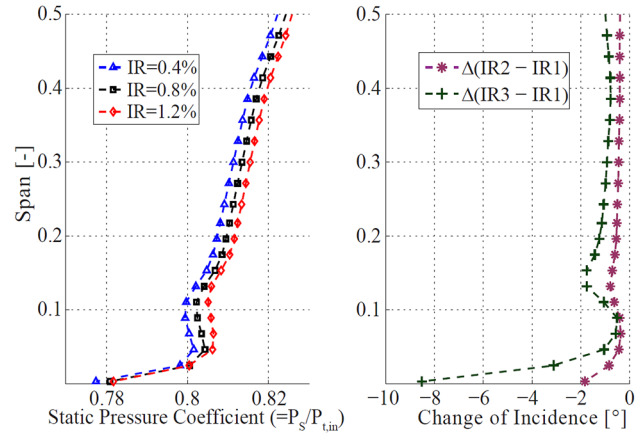


Fig. 15 Circumferentially area and time-averaged measured static pressure coefficient ($=P_s/P_{t,in}$) and change of incidence between nominal injection rate ($IR=0.8\%$) and the lowest injection rate ($IR=0.4\%$) and the maximum injection rate ($IR=1.2\%$) and the lowest injection rate at rotor inlet

pressure side separation behavior on the flow incidence angle is well known [21,22].

Conclusions

This paper presents the results of a combined experimental and computational investigation on the topic of purge flow migration and transport mechanisms in the turbine main flow containing a rotor pressure side separation. The time-resolved measurements were made in a one-and-half stage shrouded model axial turbine with profiled NGV and rotor endwalls using a fast response aerodynamic probe (FRAP). Three different levels of purge flow (0.4%, 0.8%, and 1.2%) were considered for the analysis.

The measured efficiency revealed a strong sensitivity of the total-to-total efficiency to purge flow. The experiments showed an efficiency deficit of 1.3% per injected percent of purge flow for the shrouded low-pressure turbine configuration with profiled endwalls investigated. The experiments revealed an 18% reduction of sensitivity to purge flow due to the endwall profiling. The endwall design presented successfully mitigates the interaction between purge flow and turbine hub secondary flows.

The time-resolved measurements at the rotor exit show an increase in turbulence in the hub passage vortex as a consequence of increased purge levels. The maximum root mean square values of the measured total pressure random part increase by 30% per percent of injected purge flow. The circulation of the hub passage vortex is, however, little affected by the purge flow. The variation is below 10% per percent of injected purge flow.

Furthermore, the time-resolved measurement results at the rotor exit show that the unsteady interaction between injected purge flow and the rotor flow field causes the injected purge flow to migrate to the rotor suction side. The injected purge flow leaves the rotor blade row at one circumferential region, suggesting that the migration of the purge fluid is influenced by a stationary blade row causing it to pulsate once per stator blade passing event.

CFD simulations showed a strong interaction between the size and shape of the pressure side bubble and the nozzle guide vane wake when it is convected through the rotor. Particle tracking calculations showed that the pressure side bubble fluid migrates radially towards the hub under the effect of the rotor flow field and then across the passage inside a vortical structure attached to the profiled hub endwall.

It was shown that the purge flow has a strong negative effect on the size of the pressure side bubble as it increases the static pressure by 1% per percent of injected purge flow at the rotor inlet. As

a consequence, the relative flow yaw angle decreases causing negative incidence on the airfoil stimulating the separation process.

Acknowledgment

The work leading to the results of this paper was carried out within the joint industrial and academic research program that is part of the “Luftfahrtforschungsprogramm LuFo4” supported by the German Federal Ministry of Economics and Technology. The first author would like to thank Andrea Marending from the LEC for his support with the CFD simulations.

Nomenclature

\dot{m} = mass flow (kg/s)
 p = pressure (Pa)
 \bar{p} = time mean part of pressure signal (Pa)
 \tilde{p} = periodic part of pressure signal (Pa)
 p' = random part of pressure signal (Pa)
 T = temperature (K)
 Re = Reynolds number
 IR = injection rate (%)
 N = rotational speed (r.p.s.)
 M = torque (Nm)
 T = blade passing period (s)
 t = time (s)
 V = velocity (m/s)
 U = rotational speed (m/s)
 C_p = specific heat capacity (J/kg/K)
 η = efficiency
 Π = pressure ratio
 γ = isentropic coefficient
 Ω = vorticity (1/s)

Subscripts

t = stagnation flow quantity
 s = static flow quantity
 rel = relative frame flow quantity
 tt = total-to-total
 in = turbine inlet
 red = reduced
 in = turbine inlet flow quantity
 S = streamwise

Abbreviations

FRAP = Fast Response Aerodynamic Probe
 rms = root mean square
 NGV1 = first nozzle guide vane
 NGV2 = second nozzle guide vane
 $R1$ = rotor 1
 $R1ex$ = rotor 1 exit
 $S1$ = stator 1
 $S1ex$ = stator 1 exit
 $S2$ = stator 2
 CFD = computational fluid dynamics

References

- [1] Riollet, G., 1970, “Curved Channels Through Which a Gas or Vapor Flows,” U. S. Patent No. 3529631.
- [2] Rose, M. G., 1994, “Non-Axisymmetric Endwall Profiling in the HP NGVs of an Axial Flow Gas Turbine,” Proceedings of the ASME Turbo Expo, Paper No. 94-GT-249.
- [3] Hartland, J. C., Gregory-Smith, D. G., Harvey, N. W., and Rose, M. G., 2000, “Non-Axisymmetric Turbine End Wall Design: Part II—Experimental Validation,” *Trans. ASME J. Turbomach.*, **122**(2), pp. 286–293.
- [4] Ingram, G. L., Gregory-Smith, D. G., Rose, M. G., Harvey, N. W., and Brennan, G., 2002, “The Effect of End-Wall Profiling on Secondary Flow and Loss Development in a Turbine Cascade,” Proceedings of the ASME Turbo Expo, Paper No. GT2002-30339.
- [5] Brennan, G., Harvey, N. W., Rose, M. G., Fomison, N., and Taylor, M. D., 2003, “Improving the Efficiency of the Trent 500 HP Turbine Using

- Non-Axisymmetric End Walls: Part I: Turbine Design,” *Trans. ASME J. Turbomach.*, **125**(3), pp. 497–504.
- [6] Rose, M. G., Harvey, N. W., Seaman, P., Newman, D. A., and McManus, D., 2001, “Improving the Efficiency of the Trent 500 HP Turbine Using Non-Axisymmetric End Walls: Part II: Experimental Validation,” Proceedings of the ASME Turbo Expo, Paper No. GT2001-0505.
- [7] Duden, A., Raab, I., and Fottner, L., 1999, “Controlling the Secondary Flow in a Turbine Cascade by 3D Airfoil Design and Endwall Contouring,” *Trans. ASME J. Turbomach.*, **121**(2), pp. 191–199.
- [8] Praisner, T. J., Allen-Bradley, E., Grover, E. A., Knezevici, D. C., and Sjolander, S. A., 2007, “Application of Non-Axisymmetric Endwall Contouring to Conventional and High-Lift Turbine Airfoils,” Proceedings of the ASME Turbo Expo, Paper No. GT2007-27579.
- [9] Schuepbach, P., Rose, M. G., Abhari, R. S., Germain, T., Raab, I., and Gier, J., 2008, “Improving Efficiency of a High-Work Turbine Using Non-Axisymmetric Endwalls. Part II: Time-Resolved Flow Physics,” Proceedings of the ASME Turbo Expo, Paper No. GT2008-50470.
- [10] Germain, T., Nagel, M., Raab, I., Schuepbach, P., Rose, M. G., and Abhari, R. S., 2010, “Improving Efficiency of a High-Work Turbine Using Non-Axisymmetric Endwalls. Part I: Endwall Design and Performance,” *Trans. ASME J. Turbomach.*, **132**(2), p. 021007.
- [11] Kobayashi, N., Matsumoto, M., and Shizuya, M., 1984, “An Experimental Investigation of a Gas-Turbine Disk Cooling System,” *Trans. ASME J. Eng. Gas Turbines Power*, **106**(1), pp. 136–141.
- [12] Chew, J. W., Dadkhah, S., and Turner, A. B., 1992, “Rim Sealing of Rotor-Stator Wheelspaces in the Absence of External Flow,” *Trans. ASME J. Turbomach.*, **114**(2), pp. 433–438.
- [13] Dadkhah, S., Turner, A. B., and Chew, J. W., 1992, “Performance of Radial Clearance Rim Seals in Upstream and Downstream Rotor-Stator Wheelspaces,” *Trans. ASME J. Turbomach.*, **114**(2), pp. 439–445.
- [14] McLean, C., Camci, C., and Glezer, B., 2001, “Mainstream Aerodynamic Effects Due to Wheel-space Coolant Injection in a High-Pressure Turbine Stage: Part II—Aerodynamic Measurements in the Rotational Frame,” *Trans. ASME J. Turbomach.*, **123**(4), pp. 697–703.
- [15] Ong, J. H. P., Miller, R. J., and Uchida, S., 2006, “The Effect of Coolant Injection on the Endwall Flow of a High Pressure Turbine,” Proceedings of the ASME Turbo Expo, Paper No. GT2006-91060.
- [16] Paniagua, G., Denos, R., and Almeida, S., 2004, “Effect of the Hub Endwall Cavity Flow on the Flow-Field of a Transonic High-Pressure Turbine,” *Trans. ASME J. Turbomach.*, **126**(4), pp. 578–586.
- [17] Reid, K., Denton, J., Pullan, G., Curtis, E., and Longley, J., 2006, “The Effect of Stator-Rotor Hub Sealing Flow on the Mainstream Aerodynamics of a Turbine,” Proceedings of the ASME Turbo Expo, Paper No. GT2006-90838.
- [18] Marini, R., and Girgis, S., 2007, “The Effect of Blade Leading Edge Platform Shape on Upstream Disk Cavity to Mainstream Flow Interaction of a High-Pressure Turbine Stage,” Proceedings of the ASME Turbo Expo, Paper No. GT2007-27429.
- [19] Schuepbach, P., Rose, M. G., Abhari, R. S., Germain, T., Raab, I., and Gier, J., 2010, “Effects of Suction and Injection Purge-Flow on the Secondary Flow Structures of a High-Work Turbine,” *Trans. ASME J. Turbomach.*, **132**(2), p. 021021.
- [20] Brear, M. J., Hodson, H., and Harvey, N., 2002, “Pressure Surface Separations in Low-Pressure Turbines—Part 1: Midspan Behaviour,” *Trans. ASME J. Turbomach.*, **124**(3), pp. 393–401.
- [21] Yamamoto, A., and Nouse, H., 1988, “Effects of Incidence on Three-Dimensional Flows in a Linear Turbine Cascade,” *ASME J. Turbomach.*, **110**(4), pp. 486–496.
- [22] Hodson, H., and Dominy, R., 1987, “The Off-Design Performance of a Low-Pressure Turbine Cascade,” *ASME J. Turbomach.*, **109**(2), pp. 201–209.
- [23] Brear, M. J., Hodson, H., Gonzalez, P., and Harvey, N., 2002, “Pressure Surface Separations in Low-Pressure Turbines—Part 2: Interactions With the Secondary Flow,” *ASME J. Turbomach.*, **124**(3), pp. 402–409.
- [24] Behr, T., Kalfas, A. I., and Abhari, R. S., 2007, “Unsteady Flow Physics and Performance of a One-and 1/2-Stage Unshrouded High Work Turbine,” *Trans. ASME J. Turbomach.*, **129**(2), pp. 348–359.
- [25] Germain, T., Nagel, M., and Baier, R.-D., 2007, “Visualisation and Quantification of Secondary Flows: Application to Turbine Bladings With 3D-Endwalls,” Proceedings of the ISAIF, Lyon, France.
- [26] Kupferschmid, P., Kopperl, O., Gizzi, W. P., and Gyarmathy, G., 2000, “Time Resolved Flow Measurements With Fast Aerodynamic Probes in Turbomachinery,” *Meas. Sci. Technol.*, **11**, pp. 1036–1054.
- [27] Pfau, A., Schlienger, J., Kalfas, A. I., and Abhari, R. S., 2003, “Unsteady 3-Dimensional Flow Measurement Using a Miniature Virtual 4-Sensor Fast Response Aerodynamic Probe (FRAP),” Proceedings of the ASME Turbo Expo, Paper No. GT2003-38128.
- [28] Porreca, L., Hollenstein, M., Kalfas, A. I., and Abhari, R. S., 2007, “Turbulence Measurements and Analysis in a Multistage Axial Turbine,” *J. Propul. Power*, **23**(1), pp. 227–234.
- [29] Bashforth, F., and Adams, J., 1883, *An Attempt to Test the Theories of Capillary Action by Comparing the Theoretical and Measured Forms of Drops of Fluid, With an Explanation of the Method of Integration Employed in Constructing the Tables Which Give the Theoretical Forms of Such Drops*, Cambridge University Press, Cambridge, UK.
- [30] Moore, J., 1973, “Wake and an Eddy in a Rotating, Radial-Flow Passage, Part 1: Experimental Observations,” *ASME J. Eng. Power*, **95**(3), pp. 205–212.
- [31] Greitzer, E. M., Tan, C., and Graf, M., 2004, *Internal Flow, Concepts and Applications*, 1st ed., Cambridge University Press, Cambridge, UK.